A correlated multi-observable assessment for vanadium redox flow battery state of charge estimation — Empirical correlations and temperature dependencies

Niklas Janshen [a,b,*], Simon Ressel [a], Antonio Chica [b], Thorsten Struckmann [a]

[a] *Hamburg University of Applied Sciences, Department of Mechanical Engineering and Production Managment, Berliner Tor 21, Hamburg, 20099, Germany*
[b] *Instituto de Tecnologíca Química, Universitat Polìtecnica de Valencia - Consejo Superior de Investigaciones Científicas, Avenida de los Naranjos s/n, València, 46022, Spain*
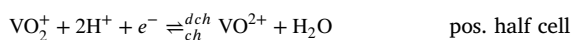
ARTICLE INFO

ABSTRACT

The efficient operation of vanadium redox flow batteries requires the half cell specific monitoring of the state of charge (SOC). Monitoring of the SOC is affected by temperature fluctuations, which need to be distinguished from the SOC signal. Several SOC monitoring approaches have been proposed in the literature and either been evaluated individually or compared to one other approach. The aim of this study is to contribute to SOC sensor development for VRFB by providing a first correlated assessment of several established and new SOC monitoring methods. We perform multi observable measurements of: half cell electrolyte potentials, electrolyte densities, electrolyte volumes, electrolyte viscosity related pressure drops, pH related potentials and UV/Vis absorbances. We determine SOC correlations of these observables in full charge/discharge cycles at constant temperature and derive temperature corrections in additional measurements over a range of 12 °C to 32 °C at 25 %, 50 % and 75 % SOC. We compare the SOC and temperature sensitivity as well as the accuracy of these monitoring methods at constant and varied temperature. We find that the established half cell electrolyte potentials and UV/Vis absorbances can estimate the SOC at constant temperature with measurement errors of 1.7% and 4%, respectively and with slightly higher errors at varying temperatures. The viscosity related pressure drop and electrolyte density are both suitable for SOC estimation if temperature corrections are included. The pH related potentials for the positive half cell and both half cell electrolyte volumes could be used for a rough SOC estimate, but need accurate temperature corrections and further long term stability evaluation.

1. Introduction

The transition of the energy supply from fossil fuels to renewable resources is accompanied by the need for reliable energy storage facilities. Redox flow batteries (RFB) are a promising storage technology due to their long durability and their independent scalability of power and capacity. RFBs are especially suitable for medium term but also for long term storage systems. While a large variety of inorganic and organic RFB chemistries are studied in the literature and a couple of them are at the threshold of commercial application, the vanadium redox flow battery (VRFB) introduced by Skyllas-Kazacos et al. [1,2] is still the most developed RFB and prevalent in commercial implementations [3–5].

The VRFB redox reactions involve only vanadium oxidation states:

$$VO_2^+ + 2H^+ + e^- \rightleftharpoons_{ch}^{dch} VO^{2+} + H_2O \qquad \text{pos. half cell}$$

$$V^{2+} \rightleftharpoons_{ch}^{dch} V^{3+} + e^- \qquad \text{neg. half cell} \qquad (1)$$

and avoid irreversible cross contamination of half cell redox couples. However, reversible electrolyte crossover through the membrane can lead to electrolyte imbalances between the battery half cells. The resulting capacity fade and possibly high half cell overpotentials during battery operation are lowering the battery efficiency and increase degradation effects. For a long term stable and efficient battery operation a battery management system with reliable and cost efficient monitoring techniques is needed [6,7]. To detect electrolyte imbalances, the state of charge (SOC) of each half cell should be monitored separately at any point in time [8]:

$$SOC = \frac{Q(t)}{Q_{max}(t)}. \qquad (2)$$

---

* Corresponding author at: Hamburg University of Applied Sciences, Department of Mechanical Engineering and Production Managment, Berliner Tor 21, Hamburg, 20099, Germany.
E-mail addresses: Niklas.Janshen@haw-hamburg.de (N. Janshen), achica@itq.upv.es (A. Chica), Thorsten.Struckmann@haw-hamburg.de (T. Struckmann).

The SOC relates the actually available amount of charge $Q(t)$ and the capacity $Q_{max}(t)$, the maximum available amount of charge. The half cell specific SOCs of the VRFB depend on the concentrations of the vanadium ions, $c_{V^{2+}}/c_{V^{3+}}$ in the negative and $c_{VO_2^+}/c_{VO^{2+}}$ in the positive half cell:

$$SOC_n = \frac{c_{V^{2+}}}{c_{V^{2+}} + c_{V^{3+}}} \tag{3}$$

$$SOC_p = \frac{c_{VO_2^+}}{c_{VO^{2+}} + c_{VO_2^+}}. \tag{4}$$

Even though a large variety of sensor approaches have been proposed in the literature, a reliable and cost efficient, in situ half cell SOC monitoring technique is still not found [8]. In addition, temperature fluctuations can have a high impact on the observable measured by the SOC sensor. Thus, sensors need to be able to distinguish the temperature effects from SOC changes.

In the following, we give a literature overview for the SOC monitoring approaches implemented in our study. For a detailed review on this topic, we refer to [8].

Potentiometric titration relies on the ex situ electrochemical determination of the vanadium redox state concentrations in each half cell. This method is often used for measuring reference SOCs but is hardly appropriate for in situ SOC monitoring due to its experimental effort. The common procedure using potassium permanganate is described by several authors in [9–11] while an alternative procedure using Ce(IV) is mentioned by Roznyatovskaya et al. [12].

Coulomb counting is an often and easily implemented in situ measurement approach since it only requires an amperemeter and calculates SOC changes by considering the transferred charge. However, the accuracy of this method in long term battery SOC monitoring is strongly limited as capacity losses due to side reactions and crossover are neglected. In addition, errors from inaccurate current measurement and integration accumulate over time.

UV/Vis absorbance and transmittance measurements utilize the concentration dependence of the different vanadium ions in the UV and visible spectrum. This method, can be implemented in situ but suffers from a high instrumental effort including lamps, measurement cells and spectrometers. Early studies on the absorbance in dependence of the molar fraction of the vanadium redox couples from Blanc et al. on VO^{2+}/VO_2^+ [13] and Heintz and Illenberger on V^{2+}/V^{3+} [14] have been extended by Tang et al. [15], Skyllas-Kazacos et al. [16], Brooker et al. [17], the research group from Limerick [18–21], Shin et al. [22] and Loktinov et al. [23]. Stable linear correlations have been confirmed for the negative half cell, but in the positive half cell, the unambiguous SOC determination is complicated by a quadratic dependence of the absorption on the SOC. Measuring at two wavelengths enables the SOC determination [21], but would require 2 calibration curves. Liu et al. [24–26] propose the usage of a full transmittance spectra as a solution for this problem.

The separate in situ measurement of half cell electrolyte potentials for half cell specific SOCs has been first performed by Skyllas and Corcuera [27]. This approach utilizes the Nernst potential dependence on the concentrations of the vanadium ions:

$$E_n^0 = E_n^{0'} + \frac{RT_n}{F} \ln\left(\frac{c_{V^{3+}}}{c_{V^{2+}}}\right) \tag{5}$$

$$E_p^0 = E_p^{0'} + \frac{RT_p}{F} \ln\left(\frac{c_{VO_2^+}}{c_{VO^{2+}}} \cdot \left(\frac{c_{H^+,p}}{c_{H_{ref}^+}}\right)^2\right) \tag{6}$$

where $c_{H_{ref}^+} = 1\,\mathrm{mol\,L^{-1}}$ and E_n^0 and E_p^0 correspond to the negative and positive half cell electrolyte potential, respectively. $E_{n/p}^{0'}$ refers to the respective standard potential and $c_{H^+,p}$ to the H^+-concentration in the positive half cell. While the H^+ dependency has been neglected in this first approach, it was included and combined with coulomb counting for a self consistent SOC calibration and determination by only measuring half cell electrolyte potentials in [28,29] by our research group.

A similar approach, using standard potentials based on the arithmetic mean of the measured potentials at the charged and discharged state of the first charge/discharge cycle, was used by Haisch et al. [30,31] to consider crossover effects. The Open Circuit Voltage (OCV), here denoted as E^0, corresponds to the difference of the half cell electrolyte potentials:

$$E^0 = E^{0'} + \frac{RT}{F} \ln\left(\frac{c_{V^{2+}}}{c_{V^{3+}}} \cdot \frac{c_{VO_2^+}}{c_{VO^{2+}}} \cdot \left(\frac{c_{H^+,p}}{c_{H_{ref}^+}}\right)^2\right) \tag{7}$$

where $E^{0'}$ refers to the standard potential. The OCV can either be measured in intervals without current [15] or in separate 'OCV cells' [32,33]. This method can be used for SOC monitoring but cannot detect half cell imbalances.

The correlations of electrolyte densities to SOC and the concentration of vanadium oxidation states has been considered by Mousa and Skyllas-Kazacos et al. [34,35] for the first time. SOC models have been developed by our research group in [28] and linked to the state of health (SOH) in [29].

Recently, the pH in VRFB in dependence of the SOC has been measured in [36]. However, few details have been reported on the calibration and accuracy.

The correlations of electrolyte viscosities to SOC and the concentration of vanadium ions have been considered in several studies [34, 35,37–39]. Li et al. [6] have suggested an indirect method using the viscosity dependent pressure drop. In their study, ex situ determined viscosities have been calibrated to the SOC and temperature using a neural network. Their approach has been experimentally validated based on the pressure drop measured over a 15 cell stack.

Temperature dependence of SOC measurements in VRFB: Most SOC measurement quantities exhibit significant temperature dependencies as indicated in the electrolyte studies of Skyllas et al. and Mousa [34, 35] for the conductivity, viscosity and density. The temperature dependence of the standard potential has been calculated theoretically in [40] based on thermodynamics. The temperature correlation of the sound speed and the acoustic attenuation coefficient measured in the electrolyte of the positive half cell in dependence of the SOC has been considered in [41]. In other SOC monitoring studies, explicit temperature models have been given for the conductivity [27], the ultrasonic velocity in the positive half cell [42], the density [28] and the wavelength shift measured in the electrolyte of the positive half cell by an interferometer sensor [43].

We identify two research gaps in this context. First, SOC monitoring studies typically evaluate one sensor approach individually against a reference method under specific battery operation conditions which complicates the fair comparison of the approaches with respect to their suitability and accuracy. Second, the impact of temperature fluctuations on measurement errors are seldomly analyzed. The temperature sensitivity of the SOC estimations have not been reported and compared yet to the knowledge of the authors. The aim of this study is to give a contribution to closing these gaps with a multi-observable approach. We perform a correlated assessment of simultaneous measurements and calibrations of SOC observables at constant temperature. Additionally, we conduct a correlated analysis of the temperature dependency for these observables. In situ SOC measurement approaches in this study are half cell electrolyte potentials, coulomb counting, UV/Vis absorbances, electrolyte densities, electrolyte viscosity related pressure drops, pH sensor potentials and electrolyte volumes measured by fill level sensors in the electrolyte tanks. We use potentiometric titration to determine the total vanadium concentration after the calibrations to validate half cell capacities. We start with the description of the multi-observable test rig and the corresponding sensor implementations of the measurement approaches. Then, details are given for the SOC calibrations at constant temperature for both half cells and the measurement with varied temperature at different, constant SOCs. For the SOC calibration at constant temperature, results are given for reference

SOCs from half cell electrolyte potentials and coulomb counting. The in situ measured SOC quantities are individually calibrated to the reference SOCs. Then, the temperature dependence of the measurement approaches are analyzed and corresponding temperature correction models are determined. Finally, the accuracies and sensitivities of the approaches are compared for constant temperature and varied temperature with temperature corrections. To summarize, the overall aim of this study is to contribute to SOC sensor development with an objective correlated analysis of SOC estimation approaches. The comparison is based on SOC and temperature correlations, a comparison of observable sensitivities to temperature as well as SOC and an evaluation of SOC estimation accuracies.

2. Experimental

In this section, we first introduce the test rig and the investigated SOC monitoring methods. Then, we describe the experimental routines for the SOC calibration and the determination of the temperature dependency of each SOC related observable.

2.1. Description of the test rig

Main test rig components and VRFB cell: All measurements are conducted within a test rig consisting of a main electrolyte cycle and a bypass for each half cell, see Fig. 1. The test rig is placed inside a fume hood, which can be heated up/cooled down by a commercially available heating and cooling system (AC 70, Heylo). We use a planar VRFB test cell (Lab-cell, Pinflow energy storage) with a 20 cm² active membrane area and 4 cm x 5 cm flow-by graphite felt electrodes (SIGRACET, ECM130, SGL Carbon), which are heat treated by SGL Carbon. The electrode compression ratio is set to 37%. A cation exchange membrane (fumasep F10100, FUMATECH BWT GmbH) with a thickness of 100 μm separates both half cells. The electrochemical measurements are conducted by a commercial potentiostat (SP-240, Biologic). All measurements are carried out with $V^{3.5+}$ electrolyte (GfE Metalle) containing 0.8 M $VOSO_4$, 0.4 M $V_2(SO_4)_3$, 2 M H_2SO_4 and 0.05 M H_3PO_4. To prevent oxidation of the V^{2+}-ions, the test rig is purged with argon gas prior to the tests and all measurements are carried out under static argon overpressure of 50 hPa. Two custom made tanks are employed in each half cell (Winzer Laborglastechnik). The electrolyte is stirred by two magnet stirrers to avoid layer building in the tanks and is pumped through each half cell cycle by solenoidal membrane pumps (Delta optodrive, Prominent) at 40 ml min⁻¹ in each measurement. Time lags due to different electrolyte composition in the tanks during discharge/charge and the sensors are expected to be small as the VRFB is operated with a high electrolyte excess of $|I_{stoi}/I_{cell}| \approx 50$.

2.2. SOC sensors

The following SOC related observables are measured in commercial and custom made flow through fittings:

The half cell electrolyte potentials are measured currentless between $Hg/Hg_2SO_4/H_2SO_4(2\,M)$ (mercury-mercurous sulfate) reference electrodes (Sensortechnik Meinsberg) and heat treated graphite felts (SIGRACET, SGL Carbon) as described in our previous studies [28,29]. The electrodes are placed after the VRFB cell in the main cycle of the test rig and housed in custom made fittings, see Fig. 2(b).

The electrolyte densities are measured in liquid density modules (Art. No. 9060, Anton Paar, accuracy ± 0.0005 g mL⁻¹) as done in [2,3].

Electrolyte viscosity related pressure drops over graphite felts are measured as suggested in [6]. The graphite felts (SIGRACET, ECM130, SGL Carbon) are housed in custom made pressure cells, see Fig. 2(a). As discussed in [6], the viscosity is proportional to the pressure drop and can be calculated using Darcy's law and the Kozeny–Carman equation. Graphite felts with lengths of 30 mm and 20 mm are inserted into the

positive and negative half cell, respectively. The varying lengths compensate for the lower viscosity of the positive electrolyte in comparison to the negative electrolyte [6]. The graphite felt is compressed between a glass rod with an outer diameter of 5.03 mm and the pressure cell (inner diameter: 6.4 mm) to a compression of 28 %. The pressure cell is located upstream of the VRFB cell to avoid high pressures in the rest of the electrolyte cycle. The pressure is measured before and after the pressure cell with remote seal pressure sensors (EM-Technik, accuracy ± 16.25 hPa).

The UV/Vis absorbance measurements are carried out using spectrometers (AvaSpec-ULS2048CL-EVO-UA-50, Avantes) with slit sizes of 50 μm and gratings for wavelengths of 200-1100 nm. The spectrometers are connected to flow through cuvettes (UV–Vis flow cell, Pinflow energy storage) with an optical path length of 0.15 mm. The flow-through cuvettes are connected to xenon lamps (AvaLight Xe, Avantes). Fiber cables (FC-UVIR100-1-BX, Avantes) with a diameter of 100 μm are used for the optical connections. The light intensities are damped by neutral density filters (NDUV504B/NDUV506B, Thorlabs GmbH) placed in filter holders (FH-DA, Avantes) to avoid saturation of the detectors. In this study, we investigate wavelengths commonly found in the literature: 400 nm and 600 nm in the negative half cell [14,15,19,20] and 580 nm and 760 nm in the positive half cell [18–21].

The pH related potential is measured between the mercury- mercurous sulfate reference electrodes used for the half cell electrolyte potential measurements and pH electrodes (GC151-L, Sensortechnik Meinsberg) inside a custom made flow through fitting, see Fig. 2(b). Both reference electrodes are connected to a measuring amplifier (MV4010, Sensortechnik Meinsberg, accuracy ±0.25 mV). The pH sensitive membrane of the pH electrode is fully immersed in electrolyte inside the flow through fitting. Test measurements showed no influence of the flow rate in our typical operation range from 12.8 mL min⁻¹ to 40 mL min⁻¹ to the measured potential. The functionality of the pH electrodes is validated using pH buffer solutions (NBS-Puffer pH = 1.68, pH = 4.01, pH = 6.86, Sensortechnik Meinsberg). The pH of the VRFB electrolyte is expected to be negative, see [36], consequently our setup cannot be calibrated by commercially available buffer solutions. In addition, the high concentrations of vanadium and sulfate/bi-sulfate ions will have an influence on the H^+-sensitive membrane of the pH electrode, also referred to as acid error. Hence, a non standardized calibration procedure with a complex calculation of the pH value would be necessary, as done in [44] for example. In this study, we focus on the suitability of the pH related potential of the pH setup for SOC estimation, which is called 'pH potential' in the rest of the paper.

The electrolyte volume, by which we refer to the entire electrolyte in the tanks, the piping, the sensors and the half cells, is based on a fill level measured by laser distance sensors (LAR-160-5V, WayCon Positionsmesstechnik GmbH, accuracy ± 0.2 %). The laser sensors are measuring the distance to a swimmer on the electrolyte in the tanks as shown in Fig. 3.

Electrolyte temperatures are measured at two points inside the test rig. One is positioned after the VRFB cell in the bypass inside the density module (accuracy ± 0.1 °C) and is employed for the observables electrolyte density, half cell electrolyte potentials, pH potential and UV/Vis absorbance. The second temperature sensor is placed in front of the VRFB cell (Pt100, accuracy ± 0.775 °C) and is used for the observables electrolyte viscosity and electrolyte volume.

Total vanadium concentrations are measured ex situ after the SOC calibrations by potentiometric titration with 0.1 M Ce(IV)-sulfate standard solution [12] by an 888 Titrando (Metrohm AG, Germany, accuracy ± 0.001 mL). Titrations are conducted at 80 °C to increase the reaction rate as suggested in [45].

All observables are averaged using MATLAB movmean and outliers are removed if necessary with MATLAB filloutliers.
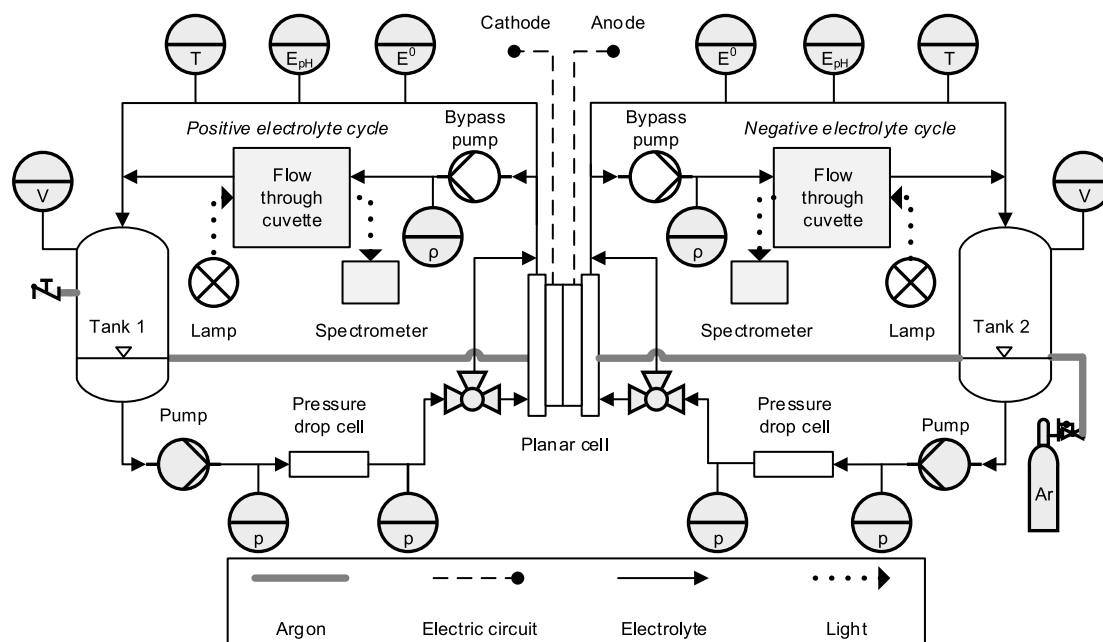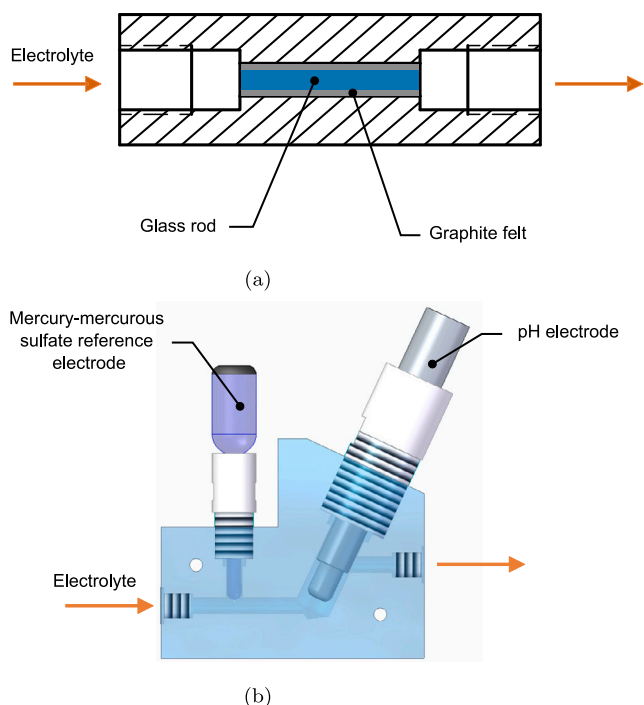
Fig. 1. Schematic of test rig.

Fig. 2. (a): Schematic of the pressure cell for the viscosity related pressure drop measurement. (b): Front view of the CAD-model of the pH flow through fitting with inserted mercury-mercurous sulfate reference and pH electrode.

Fig. 3. Schematic of custom made tank with fill level measurement.

2.3. Pre- and post measurements

Before and after each experiment, the mercury-mercurous sulfate reference electrodes are measured against another mercury-mercurous sulfate reference electrode which is permanently stored in $2\,M\,H_2SO_4$. The resulting systematic error, estimated from the recorded potential shifts, is $\approx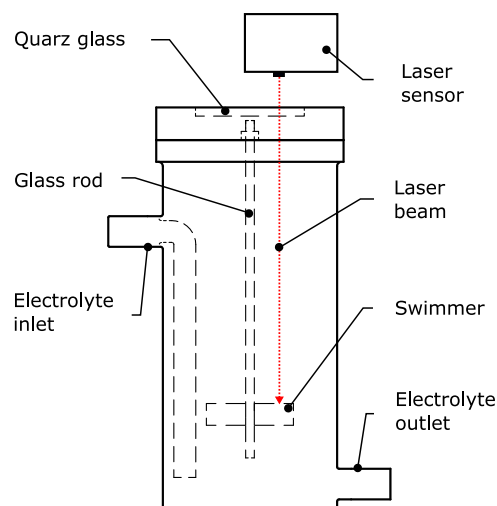 1\,mV$. The pH potential is measured in $2\,M\,H_2SO_4$ before and after each measurement. The observed potential shifts are $1\,mV$ in case of the electrodes from the negative half cell and $0.6\,mV$ in case of the positive half cell electrodes. The reference measurement for the UV/Vis absorbance is done prior to each measurement with $2\,M\,H_2SO_4$ in each flow through cuvette. In addition, a dark measurement is recorded and the absorbance A is calculated according to:

$$A = -\log\left(\frac{\iota - \iota_{dark}}{\iota_{ref} - \iota_{dark}}\right) \tag{8}$$

where ι corresponds to the measured intensity, ι_{ref} to the reference and ι_{dark} is the dark intensity. The correlation of the fill level h to the electrolyte volume V is linear and calibrated based on two steps: To determine the slope, we fill the electrolyte into the tanks in $50\,mL$ steps with $50\,mL$ full pipettes (accuracy $\pm\,0.05\,mL$). The y-intercept is determined based on a 2 min interval of constant volume flow at $40\,mL\,min^{-1}$ at the end of the pre-measurements.

2.4. SOC calibration routine

For the calibration of the observables in both half cells, two measurement runs are performed, one run with $\Delta SOC \approx 100\%$ for the negative and one run with $\Delta SOC \approx 100\%$ for the positive half cell. Each run contains the following steps: Formation and charging of 200 mL $V^{3.5+}$ electrolyte are conducted at 35 mA cm^{-2} until a charge of 8.576 A h is transferred (SOC$\approx$ 50 %). At this point, 50 mL of electrolyte are removed from the investigated half cell to ensure that this half cell is the limiting half cell and guarantee a full discharge/charge cycle. Subsequently, galvanostatic charging is done at 40 mA cm^{-2} until a cell potential of E_{cell} = 1.7 V is obtained. To reach an SOC of $\approx 100\%$ in the relevant half cell, the electrolyte is charged at E_{cell} = 1.7 V until the current density drops below 1 mA cm^{-2} and the electrolyte color changes appropriately. Next, the calibration data is generated by stepwise discharging and charging as described in [28]. In this study, the lower potential limit is set to $E_{cell} = 0.8$ V to avoid a discharge of the VRFB below 0% SOC. At the end of each calibration run, the VRFB cell is charged until $SOC \approx 50\%$ and electrolyte is withdrawn for potentiometric titration. The total vanadium concentration is determined based on three samples of 0.5 mL electrolyte.

2.5. Temperature correlation routine

The temperature dependency of all observables is investigated from 12 °C to 32 °C to cover a range equal to the temperature of the SOC calibration runs $\pm$ 10 K. The temperature dependence is measured at constant SOCs of 25 %, 50 % and 75 %. The formation and charging of 150 mL of the $V^{3.5+}$ electrolyte to SOC 50 % is done as described above, followed by a galvanostatic discharge to E_{cell} = 0.8 V. Afterwards, a charge/discharge cycle is performed at 35 mA cm^{-2} from 0.8 V to 1.6 V to let initial electrolyte changes occur in this cycle and not in the actual temperature run. At this point, the temperature run starts by charging at 35 mA cm^{-2} until a charge of 1.313 A h is transferred to reach an SOC of $\approx$ 25 %. Subsequently, the fume hood is cooled to 12 °C, followed by a heating period to 32 °C and a cooling period to room temperature. During these periods, the VRFB is bypassed to minimize the electrolyte crossover through the membrane. Each temperature period is continued until constant signals for all observables are observed. This heating and cooling sequence is repeated for SOC 50 % and SOC 75 %. In between the temperature measurements, a charge of 1.286 A h and 1.608 A h is transferred at i=35 mA cm^{-2} to reach SOC 50 % and SOC 75 %, respectively. To evaluate the influence which the temperature has on the UV/Vis setup, the UV/Vis absorbances are recorded with an empty flow through cuvette while the fume hood is heated from 22.5 °C to 40 °C. This measurement is repeated with lamps turned off to investigate the temperature influence on the detector of the spectrometer as well.

3. Results and discussion

In this section, we first calculate reference SOCs, perform SOC calibrations and derive SOC estimation equations for each investigated observable. Then, we determine the temperature corrections and analyze the sensitivity to SOC and temperature changes. Next, we assess the accuracy based on the estimation errors at constant temperature and at varied temperature with temperature correction. Finally, we evaluate each observable on their suitability for SOC estimation.

3.1. SOC calibration of observables

For the SOC calibration of the observables, we analyze two data sets: one full SOC cycle for the negative half cell, see Fig. 4(a) and one full SOC cycle for the positive half cell, see Fig. 4(b). The cell potential in Fig. 4 exhibits the stepwise discharging and charging calibration routine described in Section 2.4. The temperature during these calibrations was constant with 21.6 °C $\pm$ 0.2 °C in the negative and 21.9 °C $\pm$ 0.4 °C in the positive half cell.

Table 1

Theoretical capacities $Q_{max,n/p,fit}$, reference potentials $E_{0,n/p}'$ and RMSEs of estimated SOCs based on half cell electrolyte potentials $E_{n/p}^0$ in comparison to the reference SOC.

Negative half cell			Positive half cell		
$Q_{max,n,fit}$/A h	$E_n^{0'}$/V	$RMSE_{SOC,E_n^0}$	$Q_{max,p,fit}$/A h	$E_p^{0'}$/V	$RMSE_{SOC,E_p^0}$
6.31	−0.947	0.013	6.53	0.383	0.017

3.1.1. Reference SOC

Half cell specific reference SOCs are calibrated based on a combination of coulomb counting and half cell electrolyte potentials, as described in our previous works [28,29].

The half cell electrolyte potentials can be estimated in dependence of $SOC_{n/p}$ by combining Eqs. (3) and (4) with Eqs. (5) and (6):

$$E_n^0 = E_n^{0'} + \frac{RT_n}{F} \ln\left(\frac{1 - SOC_n}{SOC_n}\right) \tag{9}$$

$$E_p^0 = E_p^{0'} + \frac{RT_p}{F} \ln\left(\frac{SOC_p}{1 - SOC_p} \cdot \left(\frac{c_{H^+,p}(SOC_p)}{c_{H_{ref}^+}}\right)^2\right) \tag{10}$$

In the positive half cell, the half cell electrolyte potential is affected by the H^+- concentration:

$$c_{H_p^+}(SOC_p) = c_{H_{p,0}^+} + \beta \cdot c_{V_p} \cdot SOC_p. \tag{11}$$

with $c_{H_{p,0}^+} = 3$ mol L^{-1} and $\beta = 5/8$ derived from the electrolyte preparation procedure of the $V^{3.5+}$ electrolyte, the sulfuric acid concentration and dissociation [29]. The reference SOCs are determined by coulomb counting:

$$SOC_{ref,n/p}(\Delta Q) = m_{n/p} \cdot \Delta Q + SOC_{0,n/p}. \tag{12}$$

Where ΔQ corresponds to the integrated, transferred charge during the calibration runs and $SOC_{0,n/p}$ refers to the SOC at $\Delta Q = 0$. To determine the parameters $m_{n/p}$ and $SOC_{0,n/p}$, the coulomb counting approach (Eq. (12)) is inserted into the SOC dependent half cell electrolyte potentials (9) for the negative- and (10) for the positive half cell:

$$E_n^0(\Delta Q, T) = E_n^{0'} + \frac{RT_n}{F} \ln\left(\frac{1 - m_n \cdot \Delta Q - SOC_{0,n}}{m_n \cdot \Delta Q + SOC_{0,n}}\right). \tag{13}$$

$$E_p^0(\Delta Q, T) = E_p^{0'} - \frac{RT_p}{F} \ln\left(\frac{1 - m_p \cdot \Delta Q - SOC_{0,p}}{m_p \cdot \Delta Q + SOC_{0,p}}\right)$$
$$+ \frac{2RT_p}{F} \ln\left(\frac{c_{H_{p,0}^+} + \beta \cdot (m_p \cdot \Delta Q + SOC_{0,p}) \cdot c_{V_p}}{c_{H_{ref}^+}}\right) \tag{14}$$

The 3 calibration parameters $m_{n/p} = 1/Q_{max,n/p,fit}$, $SOC_{0,n/p}$ and $E_{n/p}^{0'}$ are determined by minimizing the squared residuals (MATLAB nlinfit) of the measured and estimated half cell electrolyte potentials $E_{n/p}^0(\Delta Q, T_{n/p})$. The reference SOCs are displayed in Fig. 4(c) for the negative and Fig. 4(d) for the positive half cell denoted as 'ref'. The calibration parameters are shown in Table 1. The fitted standard potentials $E_n^{0'} = -0.9467$ V and $E_p^{0'} = 0.3829$ V agree well with our previous works ($E_n^{0'} = -0.9519$ V in [28] and $E_n^{0'} = -0.9325$ V / $E_p^{0'} = 0.3898$ V in [29]).

3.1.2. SOC calibration equations and results

In the following section, we derive the calibration equations to estimate SOCs based on each observable. To analyze the quality of the SOC calibration fits, we evaluate the root mean square errors (RMSEs) of the estimated SOCs in comparison to the reference SOCs. For the calibration parameters and resulting RMSEs see Table B.1 in the appendix.

The SOCs from half cell electrolyte potentials are estimated by solving Eq. (9) for SOC_n and iteratively solving Eq. (10) for SOC_p. In each case, the standard potentials $E_{n/p}^{0'}$ determined in the 3 parameter fit, see Section 3.1.1 and the measured electrolyte temperatures $T_{n/p}$ are
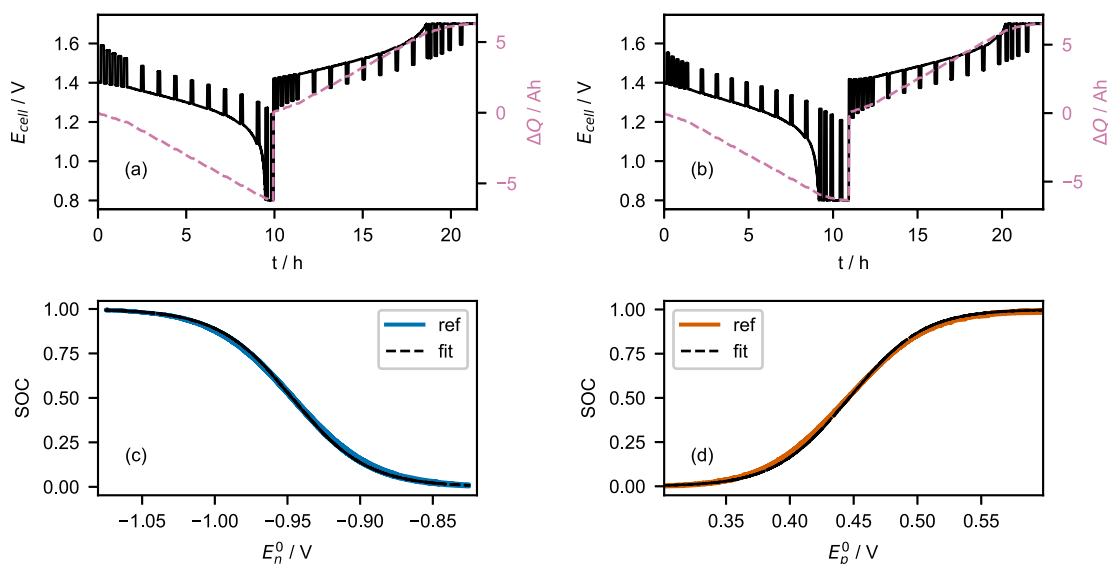
Fig. 4. Cell potential E_{cell} and transferred charge ΔQ during the calibration of the positive half cell (a) and the negative half cell (b). Reference SOC ('ref') and SOC estimated based on half cell electrolyte potentials ('fit') for the negative (c) and positive half cell (d).

used. The resulting SOCs are compared to the reference SOC in Fig. 4(c) for the negative and in Fig. 4(d) for the positive half cell denoted as 'fit'. The calibration error of $RMSE_{SOC,E_n} = 0.013$ in case of the negative half cell agrees well with our previous studies (0.013 in [28] and 0.012 in [29]). The calibration error of $RMSE_{SOC,E_p} = 0.017$ is slightly higher compared to our previous study (0.012 in [29]), but here the complete SOC range $\Delta SOC = 1$ is covered in comparison to $\Delta SOC \approx 0.5$ in [29].

The observables electrolyte density $\rho_{n/p}$, electrolyte volume $V_{n/p}$, pH potential $E_{pH,n/p}$ and UV/Vis absorbance of the negative electrolyte at wavelengths $400\,\text{nm}$ and $600\,\text{nm}$ $A_{n,400}/A_{n,600}$ depend linearly on the respective half cell SOC, see Figs. 5(a)–(f) and (i). Accordingly, the SOC based on these observables can be estimated by:

$$SOC = \lambda_1 \cdot obs + \lambda_0 \tag{15}$$

where obs refers to the respective observable. For each observable, the calibration parameters λ_1 and λ_0 are determined by minimizing the squared residuals of the estimated SOC to the reference SOC ($SOC_{ref,n/p}$). In case of the electrolyte densities, electrolyte volumes and the pH potential in the negative half cell, the SOC signals show a deviating trend for the charge in comparison to the discharge half cycle. As observed in our previous studies [28,29], the electrolyte undergoes initial changes which seem to stabilize after 3–5 charge/discharge cycles. In this paper, the accuracy analysis focuses on the short term accuracy of the investigated observables. The long term stability is beyond the scope of this paper and will be investigated in an upcoming study.

The SOCs estimated from electrolyte densities according to Eq. (15) with parameters $\lambda_{1,\rho_{n/p}}$ and $\lambda_{2,\rho_{n/p}}$ are shown in Figs. 5(a) and (b) for the negative and positive half cell, respectively. The slopes of $\lambda_{1,\rho_n} = -31.68\,\text{mL}\,\text{g}^{-1}$ and $\lambda_{1,\rho_p} = 72.63\,\text{mL}\,\text{g}^{-1}$ agree well with the slopes determined in the first charge/discharge cycles of our previous studies ($\lambda_{1,\rho_n} = -31.01\,\text{mL}\,\text{g}^{-1}$ in [28] and $\lambda_{1,\rho_n} = -34.3\,\text{mL}\,\text{g}^{-1}\,/\lambda_{1,\rho_p} = 77.4\,\text{mL}\,\text{g}^{-1}$ in [29]). In the negative half cell, the SOC signal shifts due to an overall increased density, while the SOC signal of the positive half cell shifts due to an overall lowered electrolyte density. In [29] we showed, that this shift can be used in combination with half cell electrolyte potentials to estimate the SOH of the VRFB.

The SOCs estimated from the electrolyte volume are shown in Figs. 5(c) and (d) for the negative and positive half cell, respectively. Since the electrolyte volumes are closely related to the density, they

also reflect initial electrolyte changes and show a drift from the discharge to the charge half cycle. However, we assume that this method performs better after electrolyte 'stabilization'.

In Fig. 5(e) and (f), the SOCs estimated from the pH potentials are shown. Similar, to the density and electrolyte volumes, the SOC signal for the negative half cell shows a drift from the start to the end of the calibration and exhibits a high calibration error of $RMSE_{SOC,E_{pH,n}} = 0.16$. The signal in the positive half cell shows a stable signal and a low calibration error of $RMSE_{SOC,E_{pH,p}} = 0.024$.

The SOCs estimated from the UV/Vis absorbances measured in the negative half cell at 400 nm and 600 nm are displayed in Fig. 5(i). The results agree qualitatively well with literature data [15,19] and show low calibration errors of $RMSE_{SOC,A_{n,400}} = 0.011$ and $RMSE_{SOC,A_{n,600}} = 0.027$. Reference SOCs exhibit a second order dependence on the measured pressure drops, see Fig. 5(g) and (h). The second order dependence is in agreement with the SOC depending viscosity measurements in [6]. Consequently, the SOCs can be estimated by:

$$SOC = \Delta p^2 \cdot \lambda_2 + \Delta p \cdot \lambda_1 + \lambda_0. \tag{16}$$

The calibration parameters λ_0, λ_1 and λ_2 are determined by minimizing the squared residuals of the estimated SOC to the reference SOC. The results exhibit low calibration errors of $RMSE_{SOC,\Delta p_n} = 0.017$ for the negative half cell and $RMSE_{SOC,\Delta p_p} = 0.042$ for the positive half cell. The slightly higher error in the positive half cell is attributed to the overall lower sensitivity and therefore lower signal to noise ratio. In addition, the viscosity related pressure drops show almost no shift as observed in the density, electrolyte volume and pH potential results, which makes this method more robust against initial electrolyte changes.

SOCs estimated from the UV/Vis absorbances measured in the positive half cell at wavelengths $580\,\text{nm}$ and $760\,\text{nm}$ exhibit a square root dependence, see Fig. 5(k), as shown in several other studies [18–21]. Accordingly, the absorbance can be expressed by:

$$A_p = SOC^2 \cdot a + SOC \cdot b + c \tag{17}$$

where a, b and c are regression parameters. Hence, the SOC can be estimated by:

$$SOC = \pm \sqrt{\lambda_0 + \frac{A_p}{\lambda_1}} + \lambda_2 \tag{18}$$

with

$$\lambda_0 = \frac{b^2 - 4ac}{4a^2}, \qquad \lambda_1 = a, \qquad \lambda_2 = -\frac{b}{2a}. \tag{19}$$

To assign the measured absorbance to the appropriate half of the SOC range, we evaluate the product of the algebraic sign of the cell current I_{cell} and the average of ΔA over 5 min, where $\Delta A = A_{p,580/760}(t_j) - A_{p,580/760}(t_{j+1})$ with j being the point in time:

- $I_{cell} \cdot \Delta A > 0 \rightarrow SOC > 50\%$
- $I_{cell} \cdot \Delta A < 0 \rightarrow SOC < 50\%$

For this rule to work, the OCV measurements, in which $I_{cell} = 0$, have been deleted from the data set. The estimated SOCs are shown in Fig. 5(k). Due to the definition of ΔA, the SOC estimation exhibits uncertainty close to SOC 50 as well as at SOC 0 % and 100 %, which can be seen by the vertical dashed lines in Fig. 5(k) where the estimated SOC switches back and forth between the two cases. The results agree qualitatively well with literature data [18–20] and despite the uncertainties around 0%, 50% and 100% SOC, the calibration errors are reasonably low with $RMSE_{SOC,A_{p,580}} = 0.040$ and $RMSE_{SOC,A_{p,760}} = 0.067$.

3.1.3. Titration results and crossover estimation

In this section, we discuss the measured vanadium concentrations and resulting capacities determined by titration and the corresponding electrolyte volumes, see Table 2.

Table 2
Total vanadium concentrations c_V and resulting capacities $Q_{max,titr}$ of the initial $V^{3.5+}$ electrolyte and the half cells determined by potentiometric titration and corresponding electrolyte volumes $V_{n/p}$.

	c_V/mol L^{-1}	$Q_{max,titr}$/A h
$V^{3.5+}$ electrolyte	1.61	6.49
Negative half cell	1.68	5.95
Positive half cell	1.42	6.07

The initial concentration of the $V^{3.5+}$ electrolyte corresponds to $c_V = 1.61$ mol L^{-1}, while the concentrations determined after the SOC calibrations at $SOC \approx 50\%$ are $c_{V,n} = 1.68$ mol L^{-1} for the negative and $c_{V,p} = 1.42$ mol L^{-1} for the positive half cell. The theoretical capacity of the initial electrolyte corresponds to $Q_{max,titr,V^{3.5+}} = 6.49$ A h. The transferred total charges during the calibrations measured by coulomb counting agree within 3.2 % with $Q_{max,titr,V^{3.5+}}$. The half cell capacities determined after the SOC calibrations correspond to $Q_{max,n,titr} = 5.95$ A h and $Q_{max,p,titr} = 6.07$ A h. These measured capacities agree reasonably well with the capacities $Q_{max,n,fit} = 6.31$ A h/$Q_{max,p,fit} = 6.53$ A h from the 3 parameter fit, considering that a certain amount of charge will be spent on side reactions.

When looking at the concentration and capacity results, two ambiguities need an explanation. (a): The large difference in concentration of the negative and positive half cell. (b): The small capacity difference between the half cells in contrast to the large concentration difference.

The concentration difference between the negative and positive half cell can be explained by two effects. A small part results from the density changes from the initial $V^{3.5+}$ electrolyte with a density of $\rho_{V3.5+} = 1.336$ g mL^{-1} to a higher density of the V^{2+}/V^{3+} electrolyte and a lower density of the VO^{2+}/VO_2^+ electrolyte:

$$\rho_n > \rho_{V3.5+} > \rho_p \tag{20}$$

The other part of the difference is assumed to be due to crossover and/or side reactions. In general, the higher concentration in the negative half cell agrees with the overall increased density from start to end of the calibration, see Fig. 5(a). The same holds true for the low concentration in the positive half cell and the overall decreased density, see Fig. 5(b).

The small capacity difference can be explained by the larger electrolyte volume in the positive compared to the negative half cell (see Fig. 5(c) and (d)). The first effect discussed for (a) also explains a part of the volume difference: The density changes from the $V^{3.5+}$

electrolyte to the half cell electrolytes result in a lower electrolyte volume in the negative and a higher volume in the positive half cell. The density effect on the capacity is enhanced because we withdraw 50 mL electrolyte after the formation at $SOC \approx 50\%$ when the negative electrolyte is already more dense than the positive electrolyte. The rest of the volume difference is again assumed to be due to crossover and/or side reactions.

3.2. Temperature correlations and corrections

SOC observables are well-known to be sensitive to temperature changes as mentioned in Section 1. SOC estimations with observables taken at a temperature different from the calibration temperature are thus subject to estimation errors. The aim of this subsection is to determine temperature corrections of all observables considered in Section 3.1.

In Fig. 6(a), the cell potential E_{cell} and the transferred charge ΔQ during the temperature correlation routine are shown. The charges to obtain SOCs of 25 %, 50 %, 75 % are estimated by coulomb counting. In Fig. 6(b), the temperature profiles measured in the electrolyte in front of the VRFB cell during the cooling, heating and room temperature period are shown. The jagged trends during the cooling period are due to the cooler, which was turned on and of by its controller after reaching a target temperature measured in the air. For the half cell electrolyte potentials, electrolyte volumes and pH potentials, which showed a hysteresis effect, the temperature correlation is fitted based on 3 points of constant temperature and constant observable averaged over at least two minutes at the end of each heating, cooling and room temperature period. The hysteresis can partly be contributed to the distance between the temperature sensor and the observable sensor. Another reason are the sensor temperatures which might differ from the electrolyte temperature due to different heat capacities and limited heat transfer. We determine temperature corrections by applying linear and quadratic fits to shift the observables to the mean temperature of both SOC calibrations, $T_{ref} = 21.75\,°C$. The temperature dependency of the half cell electrolyte potentials, electrolyte densities, electrolyte volumes, pH potentials and pressure drops at SOCS 25%, 50% and 75% are displayed in Fig. 7, as well as the derived temperature correction fits. The measured UV/Vis absorbances in dependence of the temperature are shown in Fig. 8. The SOC dependency of the parameters of these temperature correction has been found to be reasonably low. Therefore, the temperature correction equations are based on all three SOC measurement steps and are approximated as SOC independent. To analyze the quality of the temperature correction fits, we evaluate the RMSEs of the measured observable at temperature T in comparison to the estimated observable at this temperature. The regression parameters and the resulting RMSEs for these SOC independent corrections can be found in the appendix, see Table B.2. Half cell electrolyte potentials, electrolyte densities, electrolyte volumes, pH potentials and UV/Vis absorbances measured in the negative half cell all show a linear dependence on the temperature, see Figs. 7(a)–(h) and 8(a). Thus, we correct the observables to the reference temperature T_{ref} at each SOC individually by linear regression:

$$obs_{T_{ref},SOC} = obs_T - \tau_{1,SOC} \cdot (T - T_{ref}) \tag{21}$$

where $obs_{T_{ref},SOC}$ refers to the observable at T_{ref} and $\tau_{1,SOC}$ is the slope of the regression, both at SOC$\approx 25\%$, 50 % or 75 %. By averaging the slopes of these regressions, a temperature correction valid for all SOCs is obtained:

$$obs_{T_{ref}} = obs_T - \tau_1 \cdot (T - T_{ref}) \tag{22}$$

where τ_1 is the average of the slopes of each linear regression. The UV/Vis absorbances measured in the positive half cell show a higher order dependence on the temperature, see Fig. 8(b). For simplicity, we also apply the linear fit here. The electrolyte viscosity related pressure drops exhibit a second order dependency to the temperature,
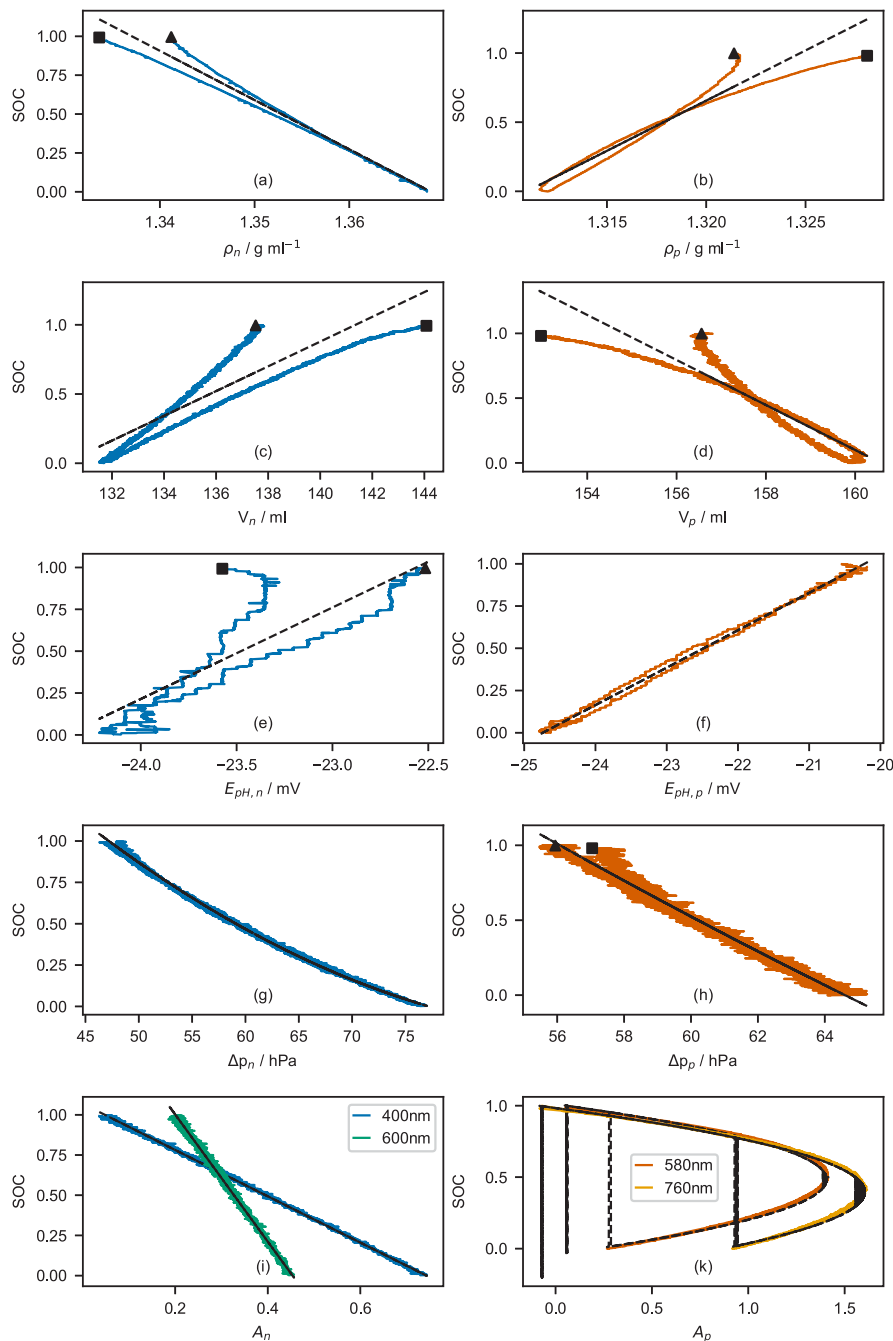
Fig. 5. $SOC_{ref,n/p}$ in dependence of measured observables: Electrolyte densities $\rho_{n/p}$ in (a)/(b), electrolyte volumes $V_{n/p}$ in (c)/(d), pH potentials $E_{pH,n/p}$ in (e)/(f), pressure drops $\Delta p_{n/p}$ in (g)/(h) and UV/Vis absorbances $A_{n/p}$ at wavelengths 400 nm and 600 nm in the negative half cell (i) and at 580 nm and 760 nm in the positive half cell (k). Start and end points of the calibration are marked by ■ and ▲, respectively. The corresponding fits are displayed as dashed lines. Negative and positive half cell observables are indicated by indices n and p, respectively.

see Fig. 7(i) and (k). Consequently, the pressure drops are corrected to T_{ref} by:

$$\Delta p_{T_{ref}} = \Delta p_T - \left[(T - T_{ref})^2 \cdot \tau_2 + (T - T_{ref}) \cdot \tau_1 \right] \tag{23}$$

where the calibration parameters τ_2 and τ_1 correspond to the average of the determined parameters from multiple linear regressions for each SOC.

Temperature dependent half cell electrolyte potentials $E^0_{n/p}$ are shown in Fig. 7(a)/(b) for the negative and positive half cell, respectively. The estimations show quite low errors with 0.000 82 mV for the negative half cell and 0.000 52 mV for the positive half cell. We find a good agreement with the literature, when we consider the slope of

the temperature dependence of the OCV ($\delta E^0/\delta T$) calculated from the measured half cell electrolyte potentials at 25 %, 50 % and 75 % SOC. We compare this slope to the value calculated based on Eqs. (7) and (11) with the temperature dependence of the standard potential of $\delta E^{0'}/\delta T = -1.26\,\text{mV K}^{-1}$ from [40] in Table 3.

Electrolyte densities $\rho_{n/p}$ depending on the temperature are displayed in Fig. 7(c) for the negative and 7(d) for the positive half cell. The slopes of $\tau_{1,\rho_n} = -0.000\,65\,\text{g mL}^{-1}\,\text{K}^{-1}$ and $\tau_{1,\rho_p} = -0.000\,67\,\text{g mL}^{-1}\,\text{K}^{-1}$ agree very well with the common slope for both half cells found in our previous study of $\tau_{1,\rho_{n/p}} = -0.000\,60\,\text{g mL}^{-1}\,\text{K}^{-1}$. Also estimation errors are quite low with 0.000 11 g mL^{-1} in the negative and 0.000 17 g mL^{-1} in the positive half cell.
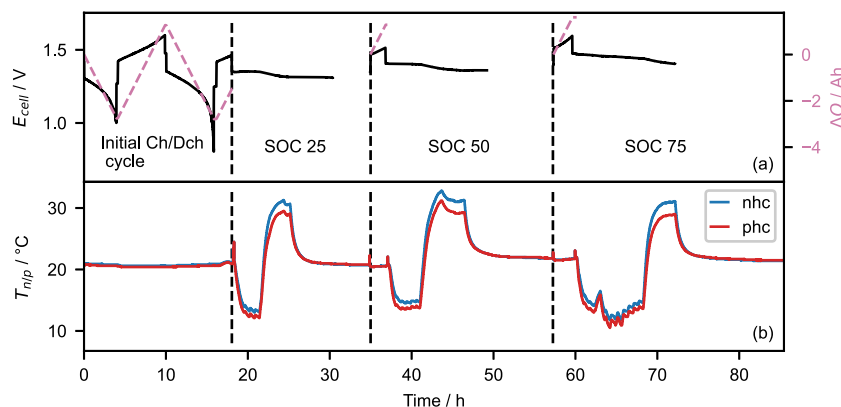
Fig. 6. (a): Cell potential E_{cell} and transferred charge ΔQ during the temperature correlation routine. (b): Temperature profile measured during the temperature correlation routine in front of the VRFB cell.

Table 3
Comparison of the slopes of the measured temperature dependencies $\delta E^0/\delta T$ of the OCV to the theoretical slope based on [40].

SOC	25 %	50 %	75 %
Theoretical $\frac{\delta E^0}{\delta T}$ / mV K^{-1}	−1.16	−1.04	−0.84
Measured $\frac{\delta E^0}{\delta T}$ / mV K^{-1}	−1.10	−0.97	−0.88

In Fig. 7(e) and (f), the electrolyte volumes $V_{n/p}$ are shown in dependence of the temperature for the negative and positive half cell, respectively. Due to an outage of the fill level signal during the measurement, we can only show the correlation for SOC 75 %. However, since the temperature dependency of the density exhibits little SOC dependency, the electrolyte volumes temperature correlation should be SOC independent as well. The estimation error for the negative half cell is very low with 0.016 mL, while the estimation error for the positive half cell corresponds to 0.16 mL.

The temperature dependence of the pH potentials $E_{pH,n/p}$ is displayed in Fig. 7(g) and (h) for the negative and positive half cell respectively. Due to a strong hysteresis effect, which we observed in the pH potential data, the estimation errors are comparatively high.

In Fig. 7(i) and (k), the pressure drops $\Delta p_{p/n}$ depending on the temperature are displayed. The second order correlation of the pressure drops to the temperature is in agreement with the viscosity measurements in [6]. The estimation errors are reasonably low with 1.1 hPa in the negative and 0.87 hPa in the positive half cell. The temperature correlations of the investigated UV/Vis absorbances are shown in Fig. 8(a) for wavelengths 400 nm and 600 nm in the negative half cell and in Fig. 8(b) for wavelengths 560 nm and 780 nm in the positive half cell. The absorbance measured at 400 nm exhibits nearly no temperature dependency, while the absorbance measured at 600 nm shows a small temperature dependence. The absorbances measured in the positive half cell exhibit an unexpected temperature influence, therefore we analyzed the behavior of the UV/Vis setup in an auxiliary measurement as described in Section 2.5. The detector alone exhibited an insignificant temperature influence, while the UV/Vis setup showed a similar nonlinear influence of the temperature on the measured intensities at the investigated wavelengths of 580 nm and 760 nm. A correction for this influence on the setup is not possible up to this point, because the temperature at the UV/Vis setup is different to the temperature measured in the electrolyte. We conclude that the UV/Vis temperature corrections in this study are only valid for our specific setup and this measurement run.

3.3. SOC sensitivity and estimation errors

In the first part of this section, we compare the sensitivities of each observable to the SOC and the temperature. In addition, we give an assessment on how sensitive the SOC estimations are to temperature variations. Second, we derive estimation errors for SOC determination at constant temperature and compare them to estimation errors of VRFB operation at varied temperatures with temperature corrected observables.

3.3.1. Temperature and SOC sensitivity of observables

We calculate the SOC and temperature sensitivities as the percentage difference of the observable per %SOC and per kelvin, respectively.

The SOC sensitivity is calculated with the slope a_{obs} of the linear regression $obs = a_{obs} \cdot SOC + b_{obs}$ and the estimated value of the observable at $SOC = 50\%$ by:

$$\frac{\Delta obs}{\Delta SOC} = \frac{a_{obs}}{obs_{SOC=50\%}} \cdot 100\%. \tag{24}$$

In case of the quadratic correlations of the UV/Vis absorbances to the SOC measured in the positive half cell, the slope is calculated as $(A_{p,w,max} - A_{p,w,min})/50\%SOC$ where w refers to the investigated wavelength.

The temperature sensitivity is calculated with the slope of the linear regression $obs = \tau_{1,SOC=50\%} \cdot T + \tau_{0,obs}$ and the value of the estimated observable at 25 °C and $SOC = 50\%$ according to:

$$\frac{\Delta obs}{\Delta T} = \frac{\tau_{1,SOC=50\%}}{obs_{T=25°C,SOC=50\%}} \cdot 100\%. \tag{25}$$

To assess the sensitivity of the SOC estimations to temperature variations, we evaluate the combined sensitivity describing the change of the SOC estimate in %SOC to a temperature shift of 1 K which turns out to be the quotient of the sensitivities: $\frac{\Delta obs}{\Delta T} / \frac{\Delta obs}{\Delta SOC} = \frac{\Delta SOC}{\Delta T}$. The results for the different sensitivities are shown in Fig. 9: the SOC sensitivity of the observables in the upper plot, the temperature sensitivity in the middle plot and the combined sensitivity in the lower plot.

The SOC estimations from the half cell electrolyte potentials exhibit little influence to temperature variations (<0.3 %). For example, the absolute shift of the SOC estimated from the negative half cell electrolyte potential would be 0.28 % with each kelvin deviation from the reference temperature T_{ref} without a temperature correction. These low influences of the temperature on the SOC estimations are contributed to the comparatively high SOC sensitivity and low temperature sensitivity of this method.

The SOC estimation based on the electrolyte density and the electrolyte volumes both show similar and higher sensitivities to the temperature. In both cases, the sensitivity of the positive half cell is
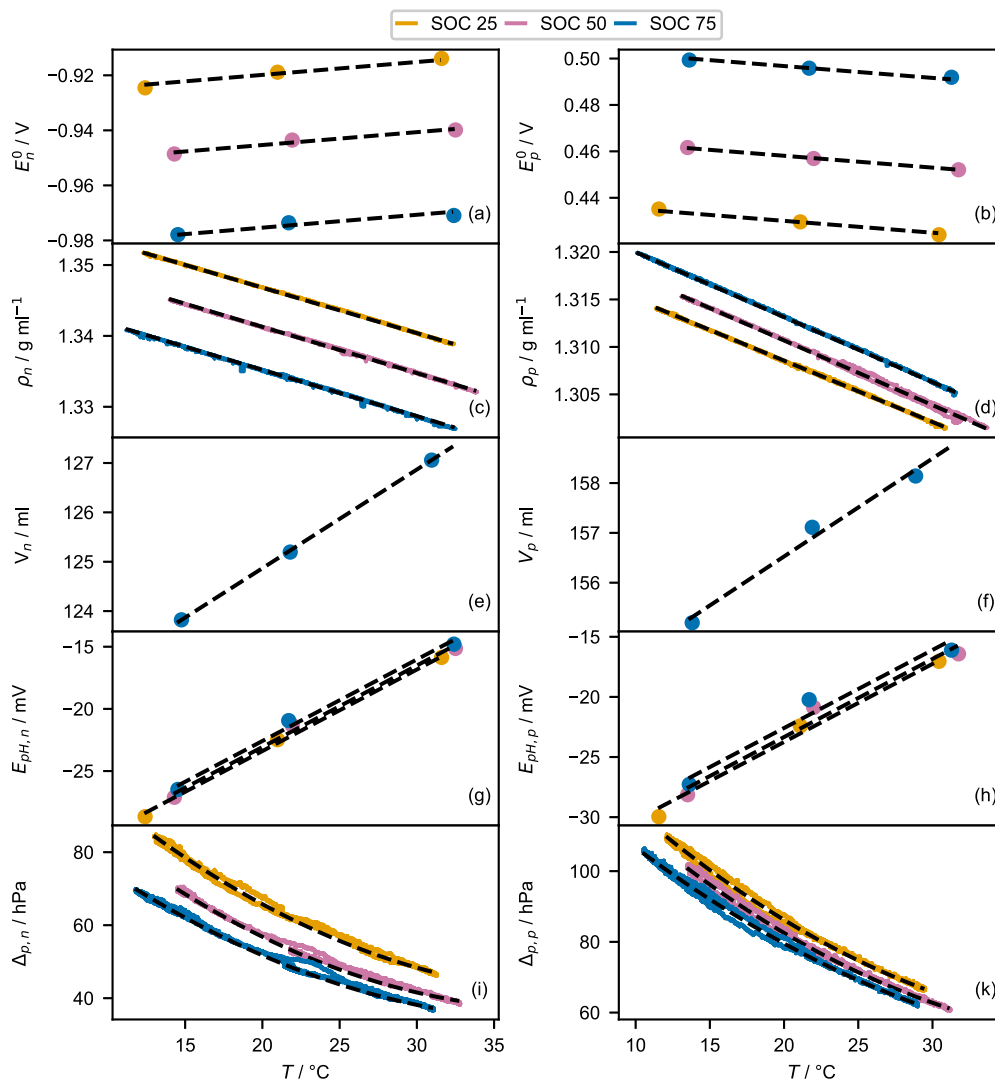
Fig. 7. Temperature dependencies of observables at 25%, 50% and 75% SOC: half cell electrolyte potentials $E^0_{n/p}$ (a)/(b), electrolyte densities $\rho_{n/p}$ (c)/(d), electrolyte volumes $V_{n/p}$ (e)/(f), pH potentials $E_{pH,n/p}$ (g)/(h) and pressure drops $\Delta p_{n/p}$ (i)/(k). The corresponding fits are displayed by dashed lines. Negative and positive half cell observables are indicated by indices n and p, respectively.
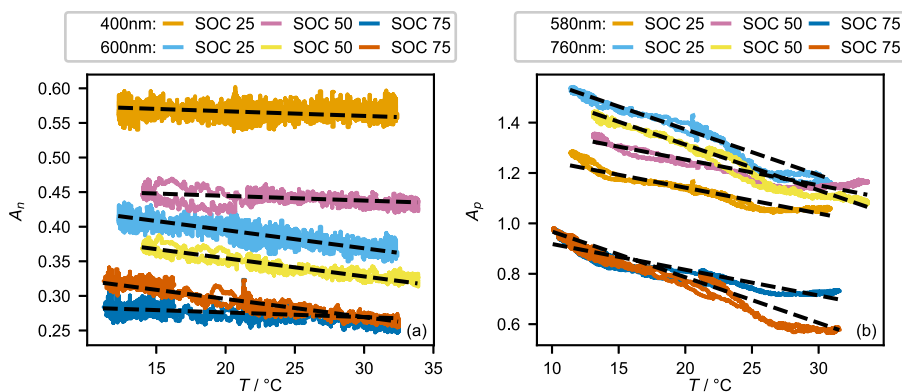
Fig. 8. Temperature dependencies of the UV/Vis absorbances measured in the negative half cell at wavelengths $400\,\text{nm}$ and $600\,\text{nm}$ (a) and in the positive half cell at $580\,\text{nm}$ and $760\,\text{nm}$ (b). The corresponding fits are displayed by dashed lines. Temperature sensitivities of the UV/Vis measurements contain a temperature influence on the UV/Vis setup and are only valid for our specific setup. Negative and positive half cell observables are indicated by indices n and p, respectively.

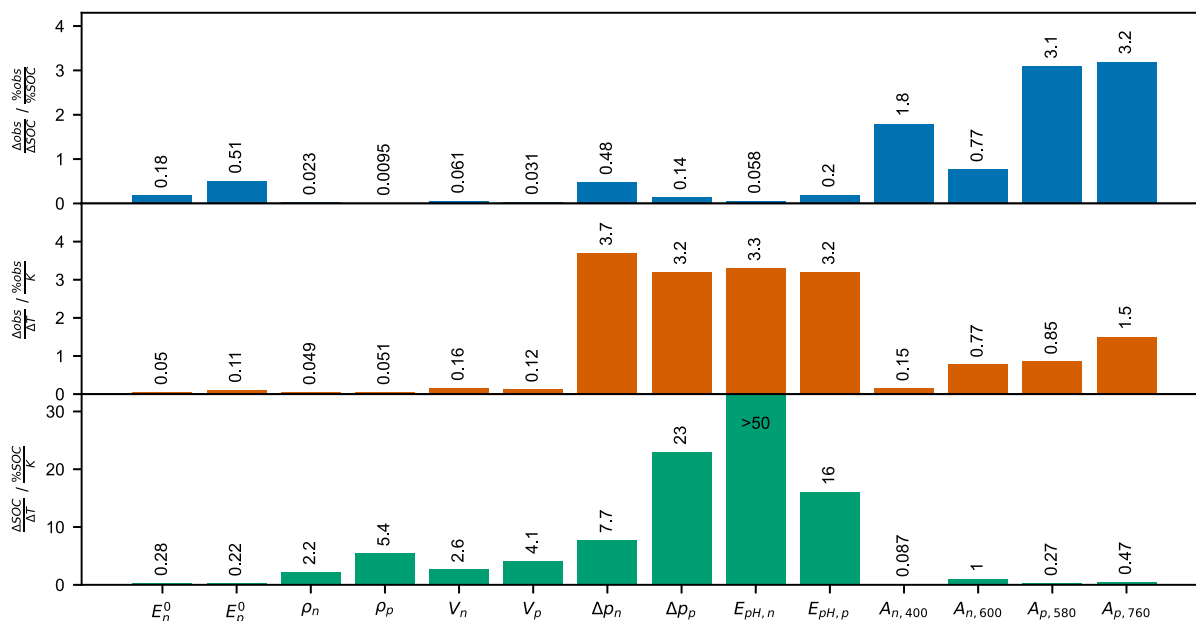**Fig. 9.** Sensitivities of observables to the SOC $\frac{\Delta obs}{\Delta SOC}$, sensitivities of observables to the temperature $\frac{\Delta obs}{\Delta T}$ and combined sensitivities $\frac{\Delta SOC}{\Delta T}$. *Temperature sensitivities of the UV/Vis measurements contain a temperature influence on the UV/Vis setup and are therefore not only related to the absorbance but to our specific setup.

approximately twice the value of the negative half cell. For example, the sensitivity of the density SOC estimation is 2.2 % SOC per K in case of the negative and 5.4 % SOC per K in case of the positive half cell. The higher sensitivities of the SOC estimations to temperature changes in the positive half cell are contributed to the lower SOC sensitivity of the density and electrolyte volumes compared to the negative half cell.

The SOCs estimated from the pressure drops show a high temperature influence with 7.7 % per K in the negative and 23 % per K in the positive half cell. The higher sensitivity of the estimations in the positive half cell are also contributed to the lower SOC sensitivity of the pressure drop in this half cell.

The SOC estimates from the pH potential in the positive half cell exhibit a high sensitivity to the temperature with 16 % SOC per K. The sensitivity of the pH potential in the negative half cell is even higher (>50 %). These high sensitivities are due to the high temperature sensitivity of the pH potential in combination with the low SOC sensitivities of this approach.

The SOC estimation based on the UV/Vis absorbances measured in the negative half cell show low sensitivities to the temperature with 0.087 % SOC per K for the absorbance measured at 400 nm and 1 % SOC per K measured at 600 nm. Also the absorbances in the positive half cell at both wavelengths exhibit low sensitivities (<0.5 %). It should be noted, as mentioned in Section 3.2, that these sensitivities include the temperature effect we observed on our UV/Vis setup.

3.3.2. Accuracy of SOC estimation at constant temperature and at varied temperature

In this section, we compare the accuracy of SOC estimation at constant temperature with the accuracy at varied temperature with temperature correction based on two estimation errors: For the estimation at constant temperature, we evaluate the RMSEs of the SOC calibrations ($RMSE_{SOC}$), which were listed in Table 1 for the half cell electrolyte potentials and Table B.1 for the other observables. For the SOC estimation at varied temperature, we combine the RMSEs of the temperature corrections ($RMSE_T$), see Table B.2, with the RMSEs of

the SOC estimations via Gaußian error propagation:

$$e_{obs} = RMSE_{obs,SOC} + \frac{\delta SOC}{\delta obs} \cdot RMSE_{obs,T} \tag{26}$$

where e_{obs} is the total SOC estimation error and $\frac{\delta SOC}{\delta obs}$ is the derivative of the SOC estimation equation with respect to the observable. The results for the two sets of estimation errors are presented in Fig. 10: the errors for estimation at constant temperature are denoted as 'const. T' and the errors for the estimation at varied temperature are labeled by '± 10 K with correction'.

The SOC estimations based on the half cell electrolyte potentials show good accuracies at constant temperature (<2 %) and slightly higher errors with temperature correction.

The estimation errors of the SOC based on the electrolyte densities correspond to 5.8 % in the negative half cell at constant temperature, while the errors of the positive half cell are higher with 10 %. Considering that these estimations are based on the first charge/discharge cycle and still contain shifts due to the initial electrolyte changes, the accuracy for the negative half cell is reasonably good and both results are expected to be better after electrolyte 'stabilization'. The estimation errors for varied temperature deviate only slightly for both half cells because of the small RMSEs of the temperature corrections. The differences in accuracies between positive and negative half cell are due to the lower SOC sensitivity of the density in the positive half cell.

The estimation errors of the SOC based on the electrolyte volumes are both very high with 16 % in almost all cases. The overall high estimation errors of the electrolyte volumes reflect the initial electrolyte changes and are expected to be better after electrolyte 'stabilization'.

The accuracy of the SOC estimation based on the pressure drop in the negative half cell shows very promising results at constant temperature (<2 %), but becomes more inaccurate with varied temperature (5.8 %). The estimation based on the pressure drop in the positive half cell exhibits higher estimation errors for both constant temperature (4.2 %) and varied temperature (14 %). The lower accuracy in the positive half cell is again contributed to the lower SOC sensitivity in this half cell.
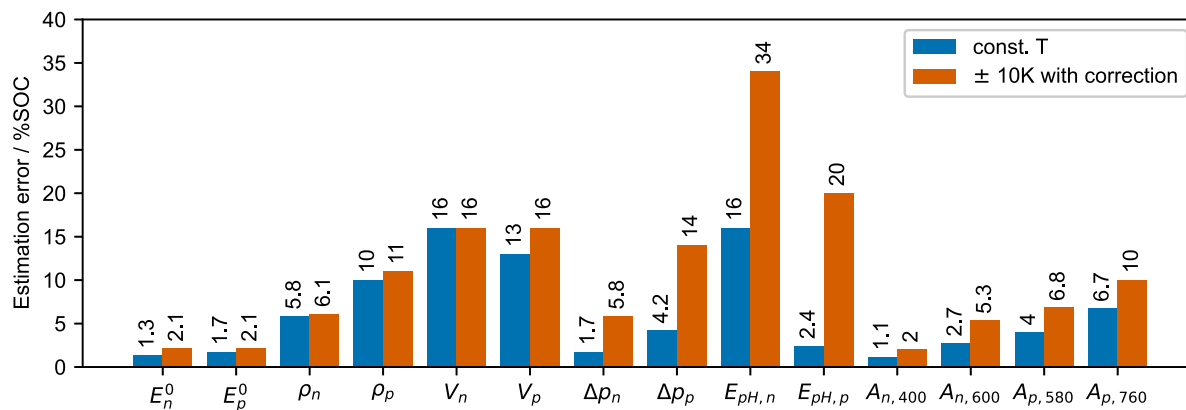
Fig. 10. Total estimation errors of SOC estimation based on the investigated observables in %SOC in case of constant temperature ('const. T') and in case of varied temperature during the temperature correlation run with temperature correction ('± 10 K with correction').

SOC estimation based on the pH potential at constant temperature in the positive half cell exhibits a low estimation error (2.4 %) and a very high error in the negative half cell (16 %). The high error in the negative half cell is due to the shift in the SOC signal and probably due to the initial electrolyte change. The large estimation errors for both half cells at varied temperature reflect the comparatively high RMSEs of the temperature correlation fits (see Table B.2) and the high sensitivity to the temperature discussed in the last section.

The accuracy of the SOC estimation based on the UV/Vis absorbances at constant temperature is very good for the negative half cell measured at 400 nm with 1.1 % and reasonably good for the estimation in the positive half cell at 580 nm with 4 %. SOC estimates with temperature correction are slightly less accurate in the negative half cell and result in larger errors in the positive half cell due to the nonlinear temperature effect we observed on our UV/Vis setup, see Section 3.2. The estimation errors for the other two wavelengths behave similarly but are in general less accurate.

3.4. Evaluation of the observables

SOC estimation based on half cell electrolyte potentials exhibits a low temperature influence and very good accuracies with estimation errors <2.1 % for both constant temperature and under high temperature variations. Therefore, temperature correction is only needed when high temperature variations are expected and should be applied depending on the accuracy demands of the SOC estimation. This method shows almost no influence to the electrolyte changes which occur in the first charge/discharge cycle which are strongly visible in most other observables. The half cell electrolyte potentials are easily and accurately measurable and the necessary reference electrodes are comparatively low-priced but necessitate the monitoring of the potential shift of the reference electrodes regularly.

The SOC estimations based on the electrolyte densities are more influenced by the temperature than estimations based on the half cell electrolyte potentials but can be corrected with good accuracy. This method is affected by initial electrolyte changes but should become more accurate after electrolyte 'stabilization' as shown in our previous studies [28,29]. Even with the inaccuracy due to the electrolyte changes, estimation errors are still decent. The dependence of the electrolyte density on the electrolyte composition can be used to estimate the SOH as shown in [28,29]. In general, the electrolyte density is an easily and very accurately measurable quantity with commercially available density modules which are comparatively expensive.

The SOC estimations based on the electrolyte volumes exhibits similar temperature influences as the electrolyte density and can be corrected with good accuracy. In general, this method suffers from high estimation errors (16 %) and needs to be re-evaluated after the long term stability is investigated. Up to this point, we can only recommend this method for a rough SOC estimation. In general, the electrolyte volume can be a valuable parameter for SOH estimation, because half cell capacities can be determined in combination with total vanadium concentrations based on in situ measured UV/Vis absorbances or ex situ by potentiometric titration. Concerning the cost of this method, our setup is relatively expensive due to the custom made tanks, but should become less costly when commercial solutions are applicable for larger tanks.

The SOC estimation via viscosity related pressure drops exhibit high temperature influences which agrees with literature data [34,35]. Temperature correction is therefore needed to achieve an accurate SOC estimation. The viscosity related pressure drops show a small influence to the initial electrolyte changes and the estimation errors should be re-evaluated after an analysis of the long term stability. In general, this method requires one additional pressure sensor as most VRFB systems will be equipped with at least one temperature and pressure sensor in each half cycle. In addition, a pressure cell is required or the pressure drop over the VRFB cell or stack itself can be utilized as done in [6]. However, in a VRFB system with variable flow rate an additional calibration step is required to determine the flow rate dependency of the pressure drop as done in [6] or the pressure drop can be measured in a bypass with constant flow rate.

The pH potential measured in the negative half cell exhibits a strong shift during the SOC calibration and shows an overall low sensitivity to the SOC of only 1.5 mV over the whole SOC range. The low sensitivity in combination with the recorded potential shift of the pH electrodes from the pre- and post measurements of 1 mV and the high estimation errors at constant temperature and at varied temperature make this method not viable. The pH potential measured in the positive half cell shows a promising accuracy at constant temperature (2.4 %) and does not seem to be influenced by initial electrolyte changes. However, the overall SOC sensitivity is still relatively low with ≈ 5 mV over the whole SOC range. The recorded potential shifts of the pH electrodes were slightly lower with 0.6 mV, but given the low SOC sensitivity still too high for an accurate SOC estimation. In addition, linear temperature correction only yields moderate accuracy. Although the necessary equipment of pH- and reference electrodes in addition to the measuring amplifier is moderately priced, it requires the potential shift monitoring of two electrodes. In general, we can only recommend the pH potential as a

rough SOC estimate in the positive half cell at constant temperatures and further research on different electrode combinations with a higher sensitivity is needed.

SOC estimation based on UV/Vis absorbances works well for the negative half cell at 400 nm as described in the literature. Due to the temperature influence we observed on our UV/Vis setup, see Section 3.2, we are only able to assess the temperature influence on our specific setup. For our setup, the absorbances exhibit a low but measurable influence for all wavelengths. The absorbances measured in the negative half cell can be corrected with good accuracy in case of 400 nm and with moderate accuracy in case of 600 nm. The temperature correction for the positive half cell is less accurate due to the nonlinear shape of the temperature correlation and the applied linear fit and should be further investigated. The measurement equipment we use in this study is comparatively expensive and for the determination of the absorbance additional reference measurements are necessary. In general, an SOC estimation with similar accuracy could be achieved only in dependence on the measured logarithmized intensities without the reference measurements.

4. Conclusions

In this study, we assess multiple in situ measured observables for SOC estimation and analyze their temperature dependency. We perform SOC calibrations based on a full charge/discharge cycle for each half cell for: half cell electrolyte potentials, electrolyte density, electrolyte volumes, viscosity related pressure drops, pH related potentials and UV/Vis absorbances. In addition, we determine the temperature correlation of each observable and derive temperature correction equations based on measurements at 25 %, 50 % and 75 % SOC for the temperature range of 12 °C to 32 °C which is equal to the temperature during the SOC calibration ± 10 K. We calculate SOC and temperature sensitivities for each observable and derive a combined sensitivity which enables us to assess the influence of temperature variations on the SOC estimation. We calculate the accuracies of the SOC estimations based on estimation errors of the SOC calibrations and the temperature correlations. We compare these errors to evaluate the accuracy for SOC estimation at constant temperature and at varying temperature (room temperature $\pm$ 10 K). Finally, we are able to compare each method and give recommendations on their applicability.

From the methods investigated in this study, the half cell electrolyte potentials and UV/Vis absorbances exhibit the highest accuracy for SOC estimation. However, the half cell potentials require monitoring of the reference electrodes and the UV/Vis absorbances need a comparatively expensive and complex measurement apparatus. The electrolyte density and electrolyte volume are both influenced by electrolyte composition changes and the accuracy needs to be re-evaluated after an analysis of the long term stability. However, due to the dependence on electrolyte composition, both observables pose a promising candidate for SOH estimation. SOC estimations based on the viscosity related pressure drops show good accuracies at constant temperatures for the negative half cell and acceptable accuracies for the positive half cell. However, this method is highly influenced by the temperature and requires a very accurate temperature correction. SOC estimation based on pH related potentials measured in the negative half cell is not recommended but can be used in the positive half cell at constant temperature.

Future research efforts will focus on the long term stability of the investigated observables and re-calibration procedures for them as well as approaches based on multiple observables for SOC and SOH estimation.

Declaration of competing interest

The authors declare that they have no known competing financial interests or personal relationships that could have appeared to influence the work reported in this paper.

Appendix A. Nomenclature

Variables

a, b, c	UV/Vis regression parameters
A	UV/Vis absorbance
c_i	Molar concentration of species i
e	Total SOC estimation error
E^0	Open circuit voltage (OCV)
$E^0_{n/p}$	Half cell electrolyte potential
$E^{0'}$	Standard potential
E_{cell}	Cell voltage
E_{pH}	pH potential
F	Faraday constant
h	Fill level
i	Current density
I_{cell}	Cell current
I_{stoi}	Stoichiometric current
m	Parameter of 3 parameter fit
$Q(t)$	Available amount of charge
Q_{max}	Capacity
R	Universal gas constant
T	Temperature
V	Electrolyte volume
β	Constant of HSO_4^- dissociation
Δ_p	Viscosity related pressure drop
ΔQ	Transferred charge
ι	Intensity
λ	SOC regression parameter
ρ	Electrolyte density
τ	Temperature correction regression parameter

Subscripts

0	Initial condition or 0
fit	Based on 3 parameter fit
n	Negative half cell
ref	Reference
$titr$	Based on titration
obs	Observable
p	Positive half cell
w	Wavelength

Appendix B. Calibration parameters

Table B.1

Regression parameters λ_0, λ_1, λ_2 and RMSEs for estimated SOCs based on electrolyte densities $\rho_{n/p}$, electrolyte volumes $V_{n/p}$, pH potentials $E_{pH,n/p}$, pressure drops $\Delta_{p,n/p}$ and UV/Vis absorbances $A_{n/p}$ at wavelengths 400 nm, 600 nm, 580 nm and 760 nm. The units of the regression parameters are consistent to the respective observable.

Obs	λ_0	λ_1	λ_2	$RMSE_{SOC}$
ρ_n/g mL^{-1}	43	−32	–	0.058
ρ_p/g mL^{-1}	−95	73	–	0.096
V_n/mL	−12	0.089	–	0.16
V_p/mL	28	−0.17	–	0.13
$E_{pH,n}$/mV	13.33	0.55	–	0.16
$E_{pH,p}$/mV	5.48	0.22	–	0.024
$\Delta p_{p,n}$/hPa	4.3	−0.093	0.00048	0.017
$\Delta p_{p,p}$/hPa	10.7	−0.22	0.00086	0.042
$A_{n,400}$	1.07	−1.44	–	0.011
$A_{n,600}$	1.79	−3.95	–	0.027
$A_{p,580}$	0.28	−5.09	0.484	0.040
$A_{p,760}$	0.34	−4.7	0.40	0.067

Table B.2

Regression parameters τ_1, τ_2 and RMSEs for temperature correction fits for half cell electrolyte potentials $E^0_{n/p}$, electrolyte densities $\rho_{n/p}$, electrolyte volumes $V_{n/p}$, pressure drops $\Delta_{p,n/p}$, pH potentials $E_{pH,n/p}$ and UV/Vis absorbances $A_{n/p}$ at wavelengths 400 nm, 600 nm, 580 nm and 760 nm. The units of the regression parameters are consistent to the respective observable.

Obs	τ_1	τ_2	$RMSE_T$
E^0_n/mV	0.00047	–	0.00082
E^0_p/mV	−0.00051	–	0.00052
ρ_n/g mL^{-1}	−0.00065	–	0.00011
ρ_p/g mL^{-1}	−0.00067	–	0.00017
V_n/mL	0.20	–	0.016
V_p/mL	0.20	–	0.16
$E_{pH,n}$/mV	0.66	–	0.34
$E_{pH,p}$/mV	0.65	–	0.80
$\Delta_{p,n}$/hPa	−1.9	0.052	1.1
$\Delta_{p,p}$/hPa	−2.3	0.048	0.87
$A_{n,400}$	−0.00068	–	0.0085
$A_{n,600}$	−0.0026	–	0.0066
$A_{p,580}$	−0.010	–	0.018
$A_{p,760}$	−0.018	–	0.022

References

[1] M. Skyllas-Kazacos, M. Rychick, R. Robins, All-vanadium redox battery, 1988 Nov 22, US Patent 4786567.

[2] M. Rychick, M. Skyllas-Kazacos, Characteristics of a new all-vanadium redox flow battery, J. Power Sources 22 (1) (1988) 59–67, http://dx.doi.org/10.1016/0378-7753(88)80005-3.

[3] J. Vinco, A. Domingos, D. Espinosa, J. Tenório, M. Baltazar, Unfolding the vanadium redox flow batteries: An indeep perspective on its components and current operation challenges, J. Energy Storage 43 (2021) 103180, http://dx.doi.org/10.1016/j.est.2021.103180.

[4] E. Sánchez-Díez, E. Ventosa, M. Guarnieri, A. Trovò, C. Flox, R. Marcilla, F. Soavi, P. Mazur, E. Aranzabe, R. Ferret, Redox flow batteries: Status and perspective towards sustainable stationary energy storage, J. Power Sources 481 (2021) 228804, http://dx.doi.org/10.1016/j.jpowsour.2020.228804.

[5] L.F. Arenas, C. Ponce de León, F.C. Walsh, Redox flow batteries for energy storage: Their promise, achievements and challenges, Curr. Opin. Electrochem. 16 (2019) 117–126, http://dx.doi.org/10.1016/j.coelec.2019.05.007.

[6] X. Li, J. Xiong, A. Tang, Y. Qin, J. Liu, C. Yan, Investigation of the use of electrolyte viscosity for online state-of-charge monitoring design in vanadium redox flow battery, Appl. Energy 211 (2018) 1050–1059, http://dx.doi.org/10.1016/j.apenergy.2017.12.009.

[7] C. Stolze, J. Meurer, M. Hager, U. Schubert, An amperometric, temperature-independent, and calibration-free method for the real-time state-of-charge monitoring of redox flow battery electrolytes, Chem. Mater. 31 (15) (2019) 5363–5369, http://dx.doi.org/10.1021/acs.chemmater.9b02376.

[8] O. Nolte, I. Volodin, C. Stolze, M. Hager, U. Schubert, Trust is good, control is better: A review on monitoring and characterization techniques for flow battery electrolytes, Mater. Horiz. 8 (7) (2021) 1866–1925, http://dx.doi.org/10.1039/d0mh01632b.

[9] M. Becker, N. Bredemeyer, N. Tenhumberg, T. Turek, Polarization curve measurements combined with potential probe sensing for determining current density distribution in vanadium redox-flow batteries, J. Power Sources 307 (2016) 826–833, http://dx.doi.org/10.1016/j.jpowsour.2016.01.011.

[10] I. Kroner, M. Becker, T. Turek, Monitoring the state of charge of the positive electrolyte in a vanadium redox-flow battery with a novel amperometric sensor, Batteries 5 (1) (2019) 5, http://dx.doi.org/10.3390/batteries5010005.

[11] J. Geiser, H. Natter, R. Hempelmann, B. Morgenstern, K. Hegetschweiler, Photometrical determination of the state-of-charge in vanadium redox flow batteries part I: In combination with potentiometric titration, Z. Phys. Chem. 233 (12) (2019) 1683–1694, http://dx.doi.org/10.1515/zpch-2019-1379.

[12] N. Roznyatovskaya, T. Herr, M. Küttinger, M. Fühl, J. Noack, K. Pinkwart, J. Tübke, Detection of capacity imbalance in vanadium electrolyte and its electrochemical regeneration for all-vanadium redox-flow batteries, J. Power Sources 302 (2016) 79–83, http://dx.doi.org/10.1016/j.jpowsour.2015.10.021.

[13] P. Blanc, C. Madic, J. Launay, Spectrophotometric identification of a mixed-valence cation-cation complex between aquadioxovanadium(v) and aquaoxovanadium(IV) ions in perchloric, sulfuric, and hydrochloric acid media, Inorg. Chem. 21 (8) (1982) 2923–2928, http://dx.doi.org/10.1021/ic00138a003.

[14] A. Heintz, C. Illenberger, Thermodynamics of vanadium redox flow batteries - electrochemical and calorimetric investigations, Ber. Bunsenges. Phys. Chem. 102 (10) (1998) 1401–1409, http://dx.doi.org/10.1002/bbpc.199800009.

[15] Z. Tang, D. Aaron, A. Papandrew, T. Zawodzinski, Monitoring the state of charge of operating vanadium redox flow batteries, ECS Trans. 41 (23) (2012) 1–9, http://dx.doi.org/10.1149/1.3697449.

[16] M. Skyllas-Kazacos, M. Kazacos, State of charge monitoring methods for vanadium redox flow battery control, J. Power Sources 196 (20) (2011) 8822–8827, http://dx.doi.org/10.1016/j.jpowsour.2011.06.080.

[17] R. Brooker, C. Bell, L. Bonville, H. Kunz, J. Fenton, Determining vanadium concentrations using the UV-Vis response method, J. Electrochem. Soc. 162 (4) (2015) A608–A613, http://dx.doi.org/10.1149/2.0371504jes.

[18] D. Buckley, X. Gao, R. Lynch, N. Quill, M. Leahy, Towards optical monitoring of vanadium redox flow batteries (VRFBs): An investigation of the underlying spectroscopy, J. Electrochem. Soc. 161 (4) (2014) A524–A534, http://dx.doi.org/10.1149/2.023404jes.

[19] X. Gao, R. Lynch, M. Leahy, D. Buckley, Spectroscopic study of vanadium electrolytes in vanadium redox flow battery (VRFB), ECS Trans. 45 (26) (2013) 25–36, http://dx.doi.org/10.1149/04526.0025ecst.

[20] N. Quill, C. Petchsingh, R.P. Lynch, X. Gao, D. Oboroceanu, D. Ni Eidhin, M. O'Mahony, C. Lenihan, D.N. Buckley, Factors affecting spectroscopic state-of-charge measurements of positive and negative electrolytes in vanadium redox flow batteries, ECS Trans. 64 (18) (2015) 23–39, http://dx.doi.org/10.1149/06418.0023ecst.

[21] C. Petchsingh, N. Quill, J. Joyce, D.N. Eidhin, D. Oboroceanu, C. Lenihan, X. Gao, R. Lynch, D. Buckley, Spectroscopic measurement of state of charge in vanadium flow batteries with an analytical model of VIV-VV absorbance, J. Electrochem. Soc. 163 (1) (2016) A5068–A5083, http://dx.doi.org/10.1149/2.0091601jes.

[22] K.-H. Shin, C.-S. Jin, J.-Y. So, S.-K. Park, D.-H. Kim, S.-H. Yeon, Real-time monitoring of the state of charge (SOC) in vanadium redox-flow batteries using UV–Vis spectroscopy in operando mode, J. Energy Storage 27 (2020) 101066, http://dx.doi.org/10.1016/j.est.2019.101066.

[23] P. Loktionov, R. Pichugov, D. Konev, M. Petrov, A. Pustovalova, A. Antipov, Operando UV/Vis spectra deconvolution for comprehensive electrolytes analysis of vanadium redox flow battery, J. Electroanal. Chem. 925 (2022) 116912, http://dx.doi.org/10.1016/j.jelechem.2022.116912.

[24] L. Liu, J. Xi, Z. Wu, W. Zhang, H. Zhou, W. Li, X. Qiu, State of charge monitoring for vanadium redox flow batteries by the transmission spectra of V(IV)/V(V) electrolytes, J. Appl. Electrochem. 42 (12) (2012) 1025–1031, http://dx.doi.org/10.1007/s10800-012-0477-2.

[25] L. Liu, J. Xi, Z. Wu, W. Zhang, H. Zhou, W. Li, Y. He, Online spectroscopic study on the positive and the negative electrolytes in vanadium redox flow batteries, J. Spectrosc. 2013 (2013) 1–8, http://dx.doi.org/10.1155/2013/453980.

[26] W. Zhang, L. Liu, L. Liu, An on-line spectroscopic monitoring system for the electrolytes in vanadium redox flow batteries, RSC Adv. 5 (121) (2015) 100235–100243, http://dx.doi.org/10.1039/C5RA21844F.

[27] S. Corcuera, M. Skyllas-Kazacos, State-of-charge monitoring and electrolyte rebalancing methods for the vanadium redox flow battery, Eur. Chem. Bull. 1 (20) (2012) 511–519.

[28] S. Ressel, F. Bill, L. Holtz, N. Janshen, A. Chica, T. Flower, C. Weidlich, T. Struckmann, State of charge monitoring of vanadium redox flow batteries using half cell potentials and electrolyte density, J. Power Sources 378 (2018) 776–783, http://dx.doi.org/10.1016/j.jpowsour.2018.01.006.

[29] T. Struckmann, P. Kuhn, S. Ressel, A combined in situ monitoring approach for half cell state of charge and state of health of vanadium redox flow batteries, Electrochim. Acta 362 (2020) 137174, http://dx.doi.org/10.1016/j.electacta.2020.137174.

[30] T. Haisch, H. Ji, C. Weidlich, Monitoring the state of charge of all-vanadium redox flow batteries to identify crossover of electrolyte, Electrochim. Acta 336 (2020) 135573, http://dx.doi.org/10.1016/j.electacta.2019.135573.

[31] T. Haisch, H. Ji, L. Holtz, T. Struckmann, C. Weidlich, Half-cell state of charge monitoring for determination of crossover in VRFB-considerations and results concerning crossover direction and amount, Membranes 11 (4) (2021) 232, http://dx.doi.org/10.3390/membranes11040232.

[32] J. Geiser, H. Natter, R. Hempelmann, B. Morgenstern, K. Hegetschweiler, Photometrical determination of the state-of-charge in vanadium redox flow batteries part II: In combination with open-circuit-voltage, Z. Phys. Chem. 233 (12) (2019) 1695–1711, http://dx.doi.org/10.1515/zpch-2019-1380.

[33] V.I. Vlasov, M.A. Pugach, D.S. Kopylova, A.V. Novikov, N.A. Gvozdik, A.A. Mkrtchyan, A.I. Davletkhanov, Y. Gladush, F.M. Ibanez, D.A. Gorin, K.J. Stevenson, In situ state of health vanadium redox flow battery deterministic method in cycling operation for battery capacity monitoring, J. Power Sources 584 (2023) 233600, http://dx.doi.org/10.1016/j.jpowsour.2023.233600.

[34] A. Mousa, Chemical and Electrochemical Studies of V (III) and V (II) Solutions in Sulfuric Acid Solution for Vanadium Battery Applications (Ph.D. thesis), University of New South Wales, 2003.

[35] M. Skyllas-Kazacos, L. Cao, M. Kazacos, N. Kausar, A. Mousa, Vanadium electrolyte studies for the vanadium redox battery-A review, ChemSusChem 9 (13) (2016) 1521–1543, http://dx.doi.org/10.1002/cssc.201600102.

[36] V. Muñoz-Perales, S. Berling, E. García-Quismondo, P.A. García-Salaberri, J. Palma, M. Vera, S.E. Ibáñez, Investigating the effects of operation variables on all-vanadium redox flow batteries through an advanced unit-cell model, J. Electrochem. Soc. 169 (10) (2022) 100522, http://dx.doi.org/10.1149/1945-7111/ac975f.

[37] M. Skyllas-Kazacos, B.M. Maddern, M. Kazacos, J. Joy, State of Charge of Redox Cell, WO1990003666A1, 1990 April 5.

[38] S. Xiao, L. Yu, L. Wu, L. Liu, X. Qiu, J. Xi, Broad temperature adaptability of vanadium redox flow battery–part 1: Electrolyte research, Electrochim. Acta 187 (2016) 525–534, http://dx.doi.org/10.1016/j.electacta.2015.11.062.

[39] Y. Yang, Y. Zhang, L. Tang, T. Liu, S. Peng, X. Yang, Improved energy density and temperature range of vanadium redox flow battery by controlling the state of charge of positive electrolyte, J. Power Sources 450 (2020) 227675, http://dx.doi.org/10.1016/j.jpowsour.2019.227675.

[40] C. Blanc, Modeling of a vanadium redox flow battery electricity storage system (Ph.D. thesis), École Polytechnique Fédérale de Lausanne, 2009, http://dx.doi.org/10.5075/epfl-thesis-4277.

[41] X. Zang, L. Yan, Y. Yang, H. Pan, Z. Nie, K.W. Jung, Z.D. Deng, W. Wang, Monitoring the state–of–charge of a vanadium redox flow battery with the acoustic attenuation coefficient: An in operando noninvasive method, Small Methods 3 (12) (2019) 1900494, http://dx.doi.org/10.1002/smtd.201900494.

[42] Y.-S. Chou, N.-Y. Hsu, K.-T. Jeng, K.-H. Chen, S.-C. Yen, A novel ultrasonic velocity sensing approach to monitoring state of charge of vanadium redox flow battery, Appl. Energy 182 (2016) 253–259, http://dx.doi.org/10.1016/j.apenergy.2016.08.125.

[43] C.-T. Ma, A novel state of charge estimating scheme based on an air-gap fiber interferometer sensor for the vanadium redox flow battery, Energies 13 (2) (2020) 291, http://dx.doi.org/10.3390/en13020291.

[44] D.K. Nordstrom, C.N. Alpers, C.J. Ptacek, D.W. Blowes, Negative pH and extremely acidic mine waters from iron mountain, California, Environ. Sci. Technol. 34 (2) (2000) 254–258, http://dx.doi.org/10.1021/es990646v.

[45] H. Willard, P. Young, Ceric sulfate as a volumetric oxidising agen VII - determination of vanadium in presence of Chromium, Tungsten and Iron, J. Am. Chem. Soc. 50 (5) (1928) 1334–1338, http://dx.doi.org/10.1021/ie50225a029.